

Influence of water saturation on the strength characteristics and deformation behavior of hardened cement paste backfill

Jie Wang (✉ 18810582761@163.com)

ustb

Jianxin Fu

USTB: University of Science and Technology Beijing

Research Article

Keywords: water saturation, cemented paste backfill, secant modulus, strength difference, box plot, fractal dimension

Posted Date: March 29th, 2021

DOI: <https://doi.org/10.21203/rs.3.rs-351748/v1>

License:   This work is licensed under a Creative Commons Attribution 4.0 International License.

[Read Full License](#)

1 Influence of water saturation on the strength characteristics and 2 deformation behavior of hardened cement paste backfill

3 Jie Wang^{1,2,*}, Jianxin Fu^{1,2,*}, Weidong Song^{1,2,*} and Yongfang Zhang^{1,2}

4 ¹ School of Civil and Resources Engineering, University of Science and Technology Beijing,
5 Beijing 100083, China

6 ² State Key Laboratory of High-Efficient Mining and Safety of Metal Mines of Ministry of
7 Education, University of Science and Technology Beijing, Beijing 100083, China

8 * Correspondence: 18810582761@163.com (J.W.); fujun0011@126.com (J.F.);
9 songwd@ustb.edu.cn (W.S.)

10 Abstract

11 In this study, a uniaxial compression experimental was conducted to examine the
12 mechanical properties of hardened cemented paste backfill (CPB) with different water
13 saturations (0.18%, 4.98%, 9.30%, 21.6%, 32.8%, and 100%). The experimental results
14 demonstrated that water saturation loosened the overall structure of the CPB, which led to the
15 deterioration of its mechanical properties. As the water saturation increased, the uniaxial
16 compressive strength (UCS), residual strength, strength difference, deformation modulus,
17 secant modulus, E_{50} (the secant modulus at 50% of the UCS), peak strain, and elastic strain
18 decreased, while the plastic strain ratio increased. The UCS, E_{50} , and peak strain demonstrated
19 exponential function relationships with the water saturation. After the peak point, when the
20 water saturation was less than 20%, the strength of the CPB decreased rapidly, and when the
21 water saturation was greater than 30%, the strength decreased slowly. Lastly, the plastic strain,
22 the strain at 50% of the UCS, and the strain at the maximum secant modulus conformed to the
23 normal distribution, and the water saturation had a minimal impact on these three strains. The
24 fractal dimension, D , of the cracks in the CPB increased exponentially with increasing water
25 saturation and demonstrated a negative linear correlation with the UCS.

26 Keywords

27 water saturation; cemented paste backfill; secant modulus; strength difference; box plot;
28 fractal dimension

29 1. Introduction

30 The stope-and-fill method of mining underground metal ore is commonly used worldwide,
31 especially in China, Canada, and Australia, because of its significant advantages in controlling
32 surface subsidence, reducing the discharge of waste rock and tailings, and making efficient use
33 of mineral resources [1-5]. Filling the mined-out area with tailings can greatly reduce the
34 exposed area of the roof, increase mining safety, improve resource recovery, and increase the
35 mine's profitability [6-10].

36 It is important to study the mechanical properties of CPB, which not only affect its
37 stability but also establish the stability of the surrounding rock and roof, thus determining the

38 safety of the mining operation [11-14]. Numerous studies, in laboratory and field-scale tests,
 39 have illustrated that the mechanical strength and stability performance of CPB is greatly
 40 affected by both internal and external parameters, especially in the presence of water [15-20].
 41 Cao et al. [21-22] analyzed the influence of structural factors (number of structural planes,
 42 angle of structural planes, and filling interval time) on the mechanical characteristics of CPB.
 43 Full et al. [23] quantitatively analyzed the influence of sulfate on the strength development of
 44 CPB and predicted the CPB's strength evolution.

45 Water is one of the most basic components of the CPB, and thus, plays a vital role [26-
 46 28]. First, it affects the efficiency of transporting the backfill slurry in the pipeline, and, second,
 47 the backfill hydration reaction requires a large amount of water [29-30]. Shortage of water can
 48 cause the cement hydration to end prematurely. However, excessive water in the CPB
 49 negatively influences its strength and durability [31-33]. As the mining continues to extend
 50 horizontally and vertically, the stope will inevitably expand to the bottom of rivers, lakes, and
 51 even the ocean [24-25]. When this occurs, excessive water penetrates the CPB along the cracks
 52 in the rock mass. When the CPB contacts excessive water, its stability changes, which can
 53 adversely impact safety. Because accurately controlling the water saturation of backfill is
 54 difficult, the existing relevant research has primarily focused on dry and fully saturated backfill
 55 [34-35]. Liu et al. [36] conducted uniaxial compression strength (UCS) tests on CPB in dried,
 56 original, and fully saturated states, and found that the strength trend was: dried state > original
 57 state > saturated state. When the CPB specimen was saturated state, the UCS was notably
 58 reduced. Hou et al. [37] analyzed the dynamic behavior of dry and water-saturated backfill and,
 59 with the help of damage mechanics theory, performed an in-depth study of the evolution of the
 60 backfill damage for both conditions.

61 Most backfill materials are exposed to humidity, and the seepage water in the cracks of
 62 the rock mass and the moisture in the air inevitably affect the mechanical properties of the
 63 backfill material. At this time, the CPB in different stopes or in different positions of the same
 64 stope is affected by different water saturation (0 to 100%). However, only studying the
 65 influence of complete drying and saturation conditions on the mechanical properties of CPB
 66 will inevitably have limitations. At present, there are relatively few studies on the effect of
 67 water saturation on the mechanical properties of backfill. The environmental conditions of the
 68 CPB vary with mines and stopes of the same mine. If we study the mechanical behavior of
 69 CPB under completely dry (water saturation of 0%) or wet (water saturation of 100%)
 70 conditions, the conclusions obtained will not be representative of most mine conditions, and
 71 this creates difficulty with providing guidance to the mines. Therefore, it is essential to study
 72 the mechanical behavior of CPB and analyze the mechanism of its strength deterioration under
 73 different water saturation conditions to provide a reference for mines to control their CPB
 74 stability.

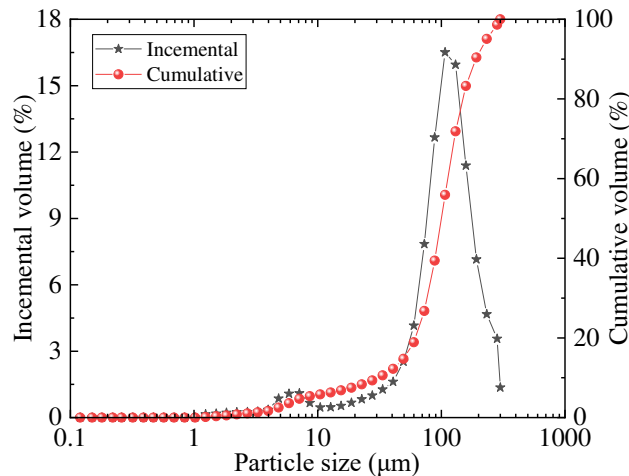
75 From the above analysis, it is of great theoretical and practical significance to study the
 76 influence of water saturation on the strength characteristics and deformation behavior of CPB.
 77 The specific objectives of this research are: firstly, to qualitatively analyze the influence of
 78 water saturation on stress-strain curve, strength characteristics and deformation behavior of
 79 hardened CPB; secondly, to quantitatively analyze the influence of water saturation and peak
 80 strength, peak strain, elastic strain and secant modulus of hardened CPB; and thirdly, to discuss
 81 the strength degradation mechanism and internal crack distribution of water-saturated CPB
 82 specimens.

83 2. Materials and Methods

84 The materials and methods section should contain sufficient detail so that all procedures
85 can be repeated. It may be divided into headed subsections if several methods are described.

86 2.1. Material characteristics

87 The tailings used in this experiment are from Shandong Province, China. The particle size
88 distribution of tailings is measured by SA-CP3 particle size analyzer (Figure1). First, the
89 tailings particles were dispersed into the coal liquid. Due to gravity, the tailings particles
90 settled, and the settling speeds of the different particle sizes were different. The differences in
91 the tailings particle settlement was obtained using the optical system. The optical signal was
92 then transformed into an electrical signal. This electrical signal was converted into data after
93 being amplified by the amplifier, and finally, the test result was output. The median particle
94 size of the tailings was 107.33 μm , and the average particle size was 144.26 μm . The weighing
95 method determined that the density of the tailings was 2.53 kg/m^3 . An x-ray diffractometer was
96 used to analyze the chemical composition of the tailings, and the results in Table 1. The binder
97 was ordinary Portland cement, type 42.5R. The test molds were transparent acrylic tubes with
98 an inner diameter of 50 mm and a height of 100 mm. The sidewall of the molds was marked
99 with a scale, and several filter holes were distributed across the bottom.



100
101 Figure 1: Incremental and cumulative PSD curves of the tailings.

102 Table 1: Chemical composition of the tailings.

Composition	SiO ₂	Al ₂ O ₃	CaO	MgO	P	Fe	S	Au
Content (%)	65.7	14.3	1.88	0.49	0.08	3.05	0.13	<0.01

103 2.2. Experimental procedures

104 2.2.1 Specimen fabrication

105 The “dry first, then wet mix” method was adopted for the CPB preparation process, to
106 make the slurry mixing more uniform. The tailings and Portland cement, type 42.5R were first
107 dry-mixed for 3 min; the proper amount of water was added, and then the mixture was stirred
108 for 3 min. The cement-to-tailings ratios of all specimens were 1:4, and the slurry concentrations
109 were 75%. The uniformly mixed slurry was poured into the molds, which were then placed in
110 a curing box having a constant temperature of 20 ± 1 °C and humidity of $95\% \pm 5$ %. After 7
111 d of curing, the CPB specimens were separated from the external molds and placed in the

112 curing box again. After a total of 60 d of curing, the 24 prepared specimens were removed from
113 the curing box to undergo further treatment.

114 2.2.2 Specimen saturation

115 CPB specimens with different amounts of water saturation were prepared as follows and
116 as shown in Figure 2:

117 (1) All the prepared specimens were placed in the constant temperature and humidity
118 curing box for natural drying for at least 2 weeks.

119 (2) The specimens were then dried for more than 6 d in a 105 °C oven, and their masses
120 were measured every 1–2 day. When the mass of a specimen no longer changed, it was
121 removed from the oven and its mass recorded as m_d .

122 (3) All specimens were placed in the laboratory and dried naturally for 1 day.

123 (4) All specimens were water-saturated under a vacuum condition, and their masses were
124 measured every 1–2 day. When the mass of a specimen no longer changed, it was removed,
125 and its mass was recorded as m_w . Before UCS testing, the mass of each specimen was
126 measured and recorded as m_i . The water saturation of the specimen is calculated as follows:

$$127 \quad w_s = \frac{m_i - m_d}{m_w - m_d} \quad (1)$$

128 where w_s is the water saturation of the specimen, m_i is the mass of the specimen before
129 compression, m_w is the mass of the specimen at full saturation, and m_d is the mass of the
130 completely dry specimen.

131 (5) Five water-saturated specimens were selected for UCS testing in water (Figure3), the
132 results of which were recorded as the group WS.

133 (6) Three water-saturated specimens were placed in the laboratory for 1 day, after which
134 the UCS testing was conducted, and the results were recorded as the group AD1.

135 (7) Five water-saturated specimens were placed in the laboratory for 2 weeks. The UCS
136 tests were then performed, and the results were recorded as the group AD.

137 (8) Three water-saturated specimens were placed in the laboratory for 2 weeks. The
138 specimens were placed in water for 30 seconds, the UCS testing was conducted, and the results
139 were recorded as the group IW.

140 (9) Three water-saturated specimens were dried in a 105 °C oven for 6 days, and the UCS
141 testing was performed, the results of which were recorded as the group OD.

142 (10) The last five water-saturated test pieces were placed in a vacuum tube for 1 day and
143 then underwent UCS testing. The results were recorded as the group VD.

Group	Number	Water saturation process	
		Step 1	Step 2
WS	5	2 weeks in curing box	UCS test in water
AD1	3	6d in oven of 105°C	1d in Lab → UCS test
AD	5		2 weeks in Lab → UCS test
IW	3	1d in Laboratory	2 weeks in Lab → 30s in water → UCS test
OD	3	Water saturation under vacuum state	6d in oven of 105 ° → UCS test
VD	5		1d in vacuum tub → UCS test

144
145 Figure 2: CPB specimen water saturation processes.



Figure 3: CPB specimens are sealed in plastic bags.

146
147

148 After the water saturation treatment, all the specimens were packaged in plastic wrap to
149 prevent environmental influence on their water saturation. Testing was conducted on the VD
150 group to verify the plastic wrap's effectiveness in isolating the specimens. After a specimen
151 was enclosed in plastic wrap and placed in the laboratory for 2 hours, a quality control test
152 showed that the mass of the specimen increased negligibly, by 0.006 g. Therefore, the plastic
153 wrap provided an effective isolation environment.

154 2.2.3 Unconfined compressive strength tests

155 The UCS test was performed on the prepared CPB specimens, which had an outer
156 diameter of 50 mm and a height of 100 mm. The equipment used was a GAW-2000 electro-
157 hydraulic servo testing machine (Figure 4). The loading rate of uniaxial compression test is
158 0.5mm/min, and the stress and strain data of CPB can be exported by Excel format.

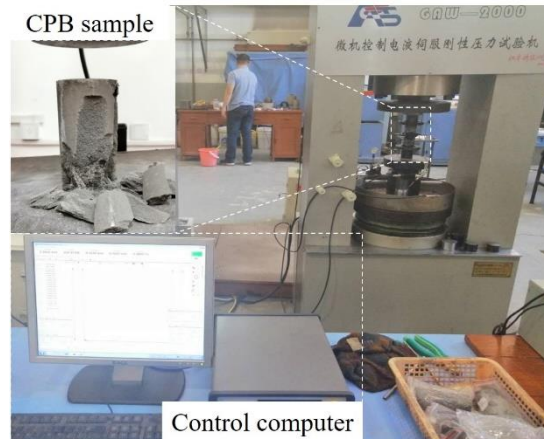


Figure 4: GAW-2000 electro-hydraulic servo testing machine.

159
160

161 3. Results and analysis

162 The primary test results of this study are shown in Table 2. The values listed are the
163 average of each group of test results. In the table, UCS is the uniaxial compressive strength;
164 σ_{res} is the residual strength; deformation modulus is the ratio of the peak stress to the strain at
165 the peak stress.

166

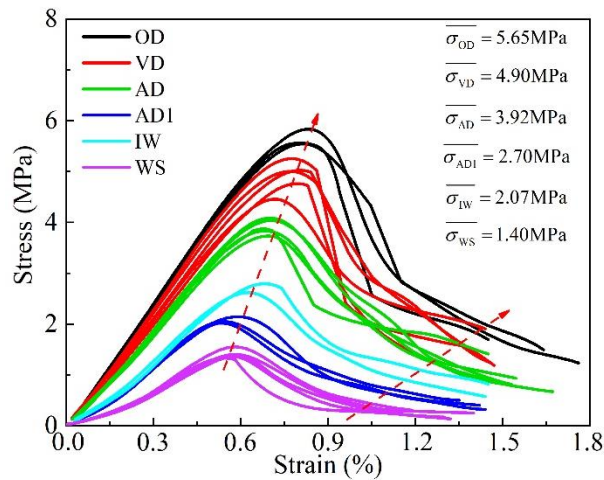
Table 2: Primary test results.

Group	w_s (%)	Deformation modulus (MPa)	UCS (MPa)	σ_{res} (MPa)
OD	0.18	699.3	5.65	1.48
VD	4.98	628.9	4.90	1.35
AD	9.30	571.4	3.92	0.947
IW	21.6	416.7	2.70	0.695

AD1	32.8	370.4	2.07	0.407
WS	100	247.6	1.40	0.212

167 3.1 Influence of water saturation on the stress-strain curve

168 The stress-strain curves for all specimens are displayed in Figure 5, and they show that,
 169 with increasing water saturation, the strength of the cemented tailings backfill gradually
 170 decreased a total of 75.2%, from the peak value of 5.65 MPa (average value) to 1.40 MPa
 171 (average value). With increasing water saturation, the slope of the curve before the peak point
 172 decreased, that is, the modulus decreased. Additionally, with increasing water saturation, the
 173 curve after the peak point changed notably. When the water saturation was less than 20%, the
 174 strength decreased rapidly after the peak point. When the water saturation was greater than
 175 30%, the strength decreased slowly after the peak point. The residual strength showed a pattern
 176 similar to that of the peak strength; with increasing water saturation, the residual strength
 177 decreased gradually. Further, the stress-strain curve of the low-saturation backfill surrounds
 178 the stress-strain curve of the high-saturation backfill.



179 Figure 5: Stress-strain curve of the specimens with different water saturation values.
 180

181 Figure 5 and Table 2 also show that the deformation modulus of the CPB decreased with
 182 increasing water saturation. When the water saturation was 0.18%, the deformation modulus
 183 of the CPB was 699.3 MPa. When the water saturation increased to 4.98%, the deformation
 184 modulus of the CPB decreased by 10.1%, to 628.9 MPa. Increasing the water saturation to
 185 9.30% decreased the deformation modulus by 9.1%, to 571.4 MPa. When the water saturation
 186 was 21.6%, the deformation modulus was 416.7 MPa, a decrease of 12%. For water saturation
 187 values of 32.8% and 100%, the deformation modulus decreased by 12% and 13%, to 370.4
 188 MPa and 247.6 MPa, respectively. Overall, when the water saturation increased from 0.18% to
 189 100%, the deformation modulus of the CPB decreased by 451.7 MPa, a reduction of 56%.

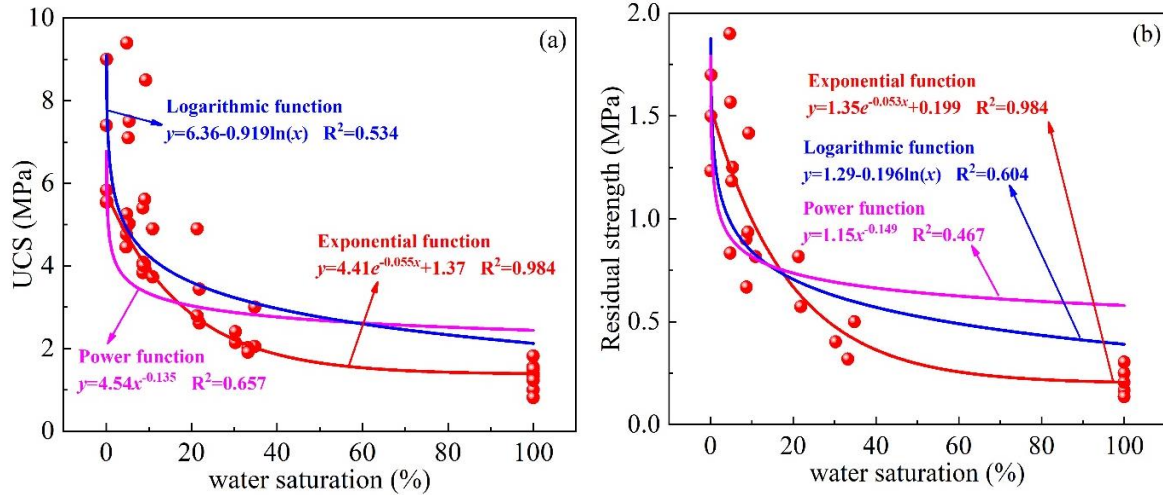
190 3.2 Influence of water saturation on strength

191 Referring to the related research results in the field of rock mechanics [38-39], this study
 192 used exponential, logarithmic, and power functions to fit and analyze the relationship between
 193 the CPB strength and water saturation. The results are shown in Figure 6.

194 Figure 6 shows that, with increasing water saturation, the UCS of the CPB decreased
 195 rapidly. The UCS was particularly sensitive to water saturation in the lower saturation range,
 196 with a slight change in water saturation causing a rapid decrease in the strength. As the water
 197 saturation increased, the sensitivity of the UCS to the water saturation decreased significantly.
 198 The residual strength demonstrated similar properties. When the water saturation increased
 199 from 0.11% to 32.8%, the uniaxial compressive strength and residual strength decreased by

200 63.4% and 72.5%, respectively; when the water saturation increased from 32.8% to 100%, the
 201 strength decreased by 32.4% and 47.9%, respectively.

202 The parameters and R2 values of the fitting functions are also provided in Figure 6, and
 203 they show that the degree of fit of the exponential function was higher than for the logarithmic
 204 and power functions. The exponential function well represents the observed characteristic of a
 205 slower strength change in the later stages, and the water saturation can be taken as zero, while
 206 the water saturation of the logarithmic and power functions cannot.



207
 208 Figure 6: Relationship between the strength and water saturation of the CPB specimens. (a) UCS. (b) residual
 209 strength.

210 3.3 Influence of the water saturation on the strain

211 It is well known that the total stress-strain curve of CPB can be divided into compaction,
 212 elastic, and plastic deformation parts prior to the peak point. [8, 40]. The strain at the peak
 213 point can be calculated with Eq. 3 if the strain produced in the compaction part is ignored, then

$$214 \quad \varepsilon_f = \varepsilon_e + \varepsilon_p \quad (3)$$

215 where ε_f is the strain at the peak point, ε_e is the elastic strain, and ε_p is the plastic strain.

216 The relationship between these three strain values and water saturation, and the
 217 relationship between the plastic strain ratio and water saturation is shown in Figure 7. The
 218 plastic strain ratio is defined as follows:

$$219 \quad \varepsilon_p^* = \varepsilon_p / \varepsilon_f \quad (4)$$

220 Three fitting function types-exponential, logarithmic, and power functions-were used to
 221 fit the relationship between the strain and water saturation; the results shown in Figure 7a-c. It
 222 can be seen from Figure 7a-b that with increasing water saturation, the peak strain and elastic
 223 strain demonstrate patterns of change similar to that of the strength. The greater the water
 224 saturation was, the lower the peak strain and elastic strain were, and, as the water saturation
 225 increased, the sensitivity of the peak strain and elastic strain to the water saturation decreased.
 226 It can be seen from Figure 7a-b that there is no clear relationship between the plastic strain and
 227 the water saturation, which is a discrete distribution, distributed between 0.00115 and 0.0019,
 228 among which the points between 0.0014 and 0.0016 are the greatest. Figure 7d shows that
 229 although the plastic strain distribution was relatively discrete, the plastic strain ratio gradually
 230 increased as the water saturation increased. In the lower water saturation interval, the plastic
 231 strain ratio increased rapidly, and when the water saturation exceeded 30%, the plastic strain
 232 ratio decreased rapidly.

233 As can also be seen from Figure 7, the exponential function had the best degree of fit for
 234 the relationships between the water saturation and the peak point and elastic strains. However,
 235 the power function had the greatest degree of fit to the relationship between the water saturation

236 and the plastic strain ratio. Based on the conclusion in Section 3.2, the strength decreased with
 237 increasing water saturation, and it can be inferred that the strength also decreased with
 238 increasing plastic strain ratio.

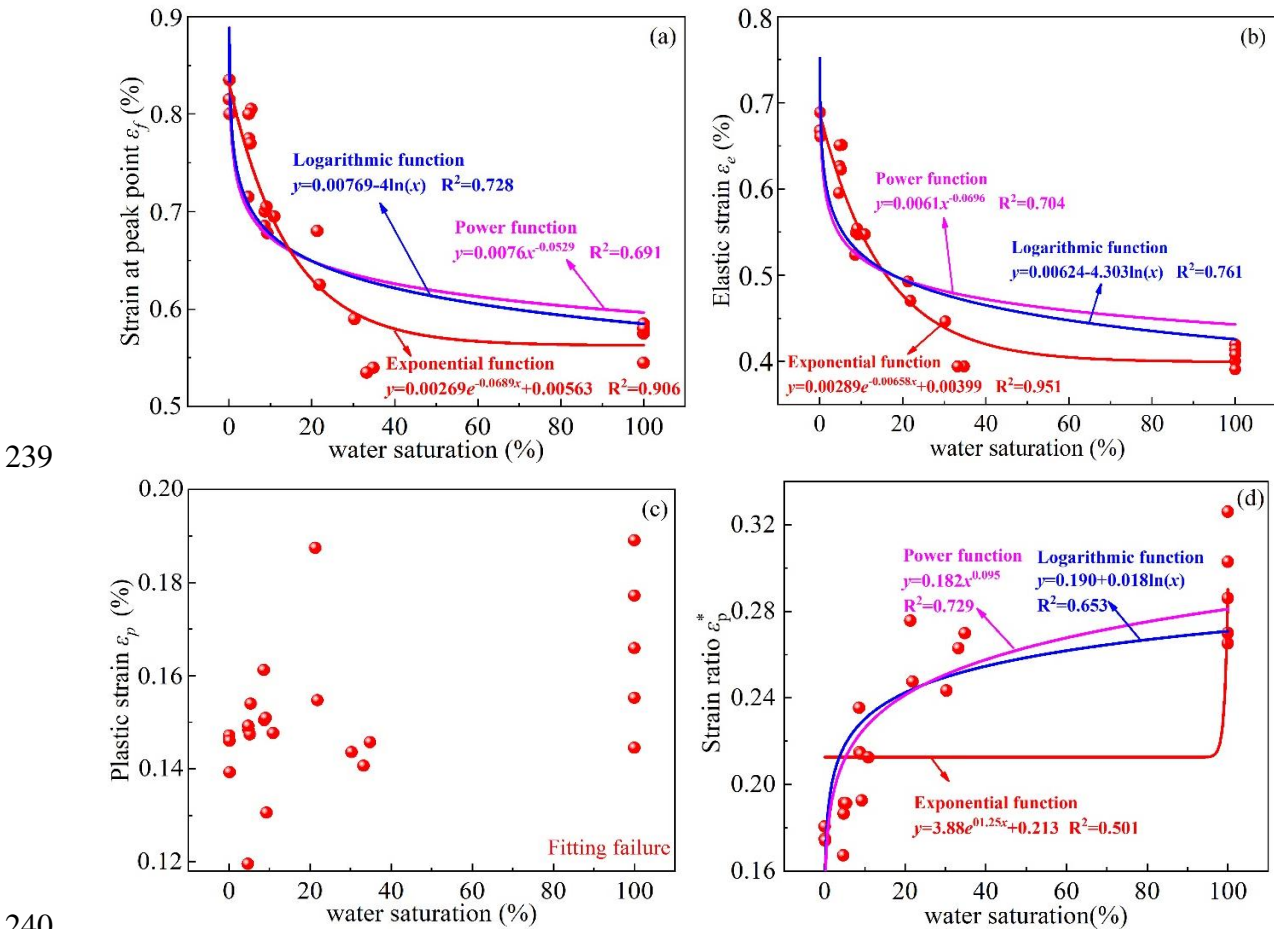


Figure 7: Relationship between the strains and water saturation. (a) ϵ_f . (b) ϵ_e . (c) ϵ_p . (d) ϵ_p^* .

242 **3.4 Influence of the water saturation on the secant modulus**

243 Secant modulus is an important backfill parameter and reflects the deformation
 244 characteristics of the backfill. One specimen from each group was chosen for studying the
 245 secant modulus. The results are shown in Figure 8.

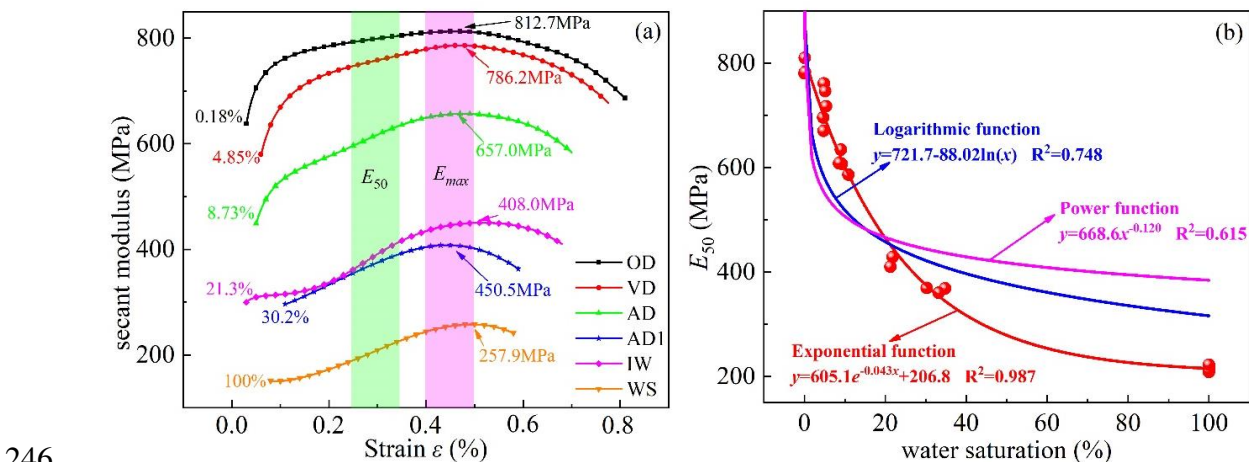


Figure 8: The evolution of the CPB modulus. (a) secant modulus. (b) E_{50} .

248 It can be seen from Figure 8a that the secant modulus decreased with increasing water
 249 saturation, and the maximum secant modulus decreased from 812.7 MPa to 257.9 MPa when

250 the water saturation increased from 0.18% to 100%, representing a decrease of 68.3%. For
 251 specimens with any water saturation, the secant modulus demonstrated a trend of first
 252 increasing and then decreasing; the critical point was 0.5%. For the specimens with water
 253 saturations of 0.18%, 4.85%, and 8.73%, the secant modulus increased rapidly at low strain,
 254 indicating that the specimens had a compression region. The secant modulus then increased
 255 slowly and remained almost unchanged, indicating that the specimen entered the stage of linear
 256 change. For the specimens with water saturations of 21.3%, 30.2%, and 100%, the secant
 257 modulus was always in the stage of uniform growth, indicating that there was no apparent
 258 compression stage in the CPB, which clearly demonstrated plastic characteristics.

259 The two columnar zones in Figure 8a are the strain ranges of E_{50} (the secant modulus at
 260 50% of the UCS) and the maximum secant modulus of each specimen. It can be seen from
 261 Figure 8a that the strain distribution was between 0.0025 and 0.0035 when the specimen
 262 reached E_{50} and between 0.004 and 0.005 when it reached the maximum secant modulus.

263 The E_{50} of each specimen was calculated as provided in Figure 8b, which shows that, with
 264 increasing water saturation, the E_{50} demonstrated a similar relationship with the strength and
 265 strain, that is, when the water saturation was low, the E_{50} was particularly sensitive to the water
 266 saturation, and the rate of change decreased as the water saturation increased. When the water
 267 saturation increased from 0.11% to 32.8%, the E_{50} decreased by 53.7%; when water saturation
 268 increased from 32.8% to 100%, the E_{50} decreased by 41.1%.

269 Exponential, logarithmic, and power functions were also used to fit the relationship
 270 between the E_{50} and water saturation. The fitting parameters and R^2 are shown in Figure 8b.
 271 The exponential function had the highest degree of fit and characterizes the rule of change of
 272 the E_{50} with water saturation better than that by logarithmic or power functions.

273 In conclusion, the water saturation had a significant effect on the mechanical properties
 274 of the CPB. With increasing water saturation, the UCS, ε_f , ε_e , and E_{50} all demonstrated an
 275 exponential function relationship, as provided in Eqs. 5-8. These results support the research
 276 of references [41-45].

$$277 \quad UCS = 4.41e^{-0.055w_s} + 1.37 \quad (5)$$

$$278 \quad E_{50} = 605.1e^{-0.043w_s} + 206.8 \quad (6)$$

$$279 \quad \varepsilon_f = 0.00269e^{-0.0689w_s} + 0.00563 \quad (7)$$

$$280 \quad \varepsilon_e = 0.00289e^{-0.0658w_s} + 0.00399 \quad (8)$$

281 4. Discussion

282 4.1 Relationship between the strength difference and water saturation

283 Based on the study results, the relationship between the uniaxial compressive strength
 284 and the water saturation of the CPB can be expressed by the exponential function shown in
 285 Eq. 9:

$$286 \quad \sigma_f(w_s) = ae^{-bw_s} + c, \quad (0 \leq w_s \leq 100) \quad (9)$$

287 where $\sigma_f(w_s)$ is the UCS of the specimen having a water saturation of w_s , and a , b , and c are
 288 constants. The parameter b is a dimensionless constant defining the rate of strength loss with
 289 increasing water content and characterizing the material's sensitivity, with larger values
 290 corresponding to more sensitive materials.

291 Parameters a and c can be obtained by testing the strength of the water-saturated and dry
 292 specimens. However, more experiments would be needed to determine b , so, for practical
 293 engineering, it is useful to simplify the method for determining this parameter.

294 Based on Eq. 9, the difference between the strength of any water saturation specimen and that
 295 of fully saturated specimens can be directly obtained as follows:

$$296 \quad \Delta\sigma_f = ae^{-bw_s} \quad (10)$$

297 Using Eq. 9, the values of a and c can be determined, and Eq. 10 can be transformed into:

$$298 \quad \Delta\sigma_f = [\sigma_f(0) - \sigma_f(100)]e^{-bw_s} \quad (11)$$

299 In the actual experimental process, there is a certain discreteness between different CPB
 300 specimens. If it is assumed that the difference between the actual strength and the experimental
 301 value, as calculated by Eq. 11, is 1% of the actual strength of the fully saturated CPB, and the
 302 specimen reaches full saturation, then:

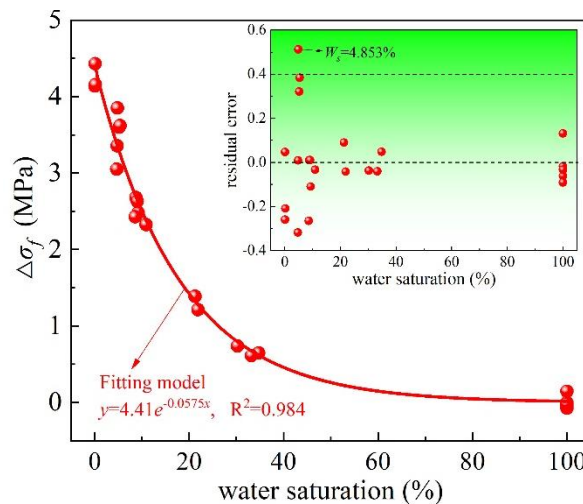
$$303 \quad e^{-100b} = \frac{1\% \times \overline{\sigma_{ws}}}{\sigma_f(0) - \sigma_f(100)} \quad (12)$$

304 Eq. 12 can be further modified to obtain:

$$305 \quad b = -\ln\left(\frac{1\% \times \overline{\sigma_{ws}}}{\sigma_f(0) - \sigma_f(100)}\right) / 100 \quad (13)$$

306 Based on the results of the experiment and fitting analysis, when the CPB was fully
 307 saturated, the average strength of the CPB specimen was 1.405 MPa, $\sigma_f(0) - \sigma_f(100) = 4.41$. From
 308 this, $b = 0.0575$ can be obtained, and the formula for the strength difference is as follows:

$$309 \quad \Delta\sigma_f = 4.41e^{-0.0575w_s} \quad (14)$$



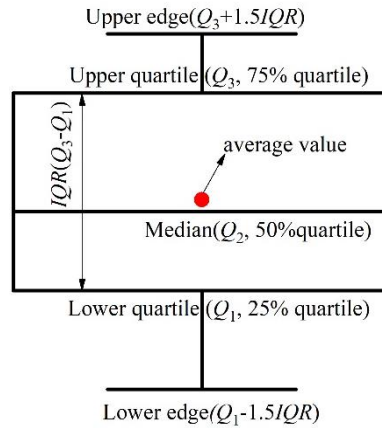
310
 311 Figure 9: Relationship between the strength difference and water saturation.

312 Eq. 14 is used for fitting and precision analysis. Figure 9 shows the fitting results between
 313 the strength difference and water saturation, and the upper right corner of Figure 9 shows the
 314 residual value after fitting. It can be observed that R^2 is 0.984 after fitting with Eq. 14, and the
 315 residual distribution is $(-0.4, +0.4)$. Only one abnormal point was noted, when the water
 316 saturation is 4.853%, illustrating the extremely high degree of fit of Eq. 14. Therefore, in
 317 mining engineering, Eq. 14 can be used to predict the strength of CPBs having different water
 318 saturations.

319 4.2 Interdependency of strain and water saturation

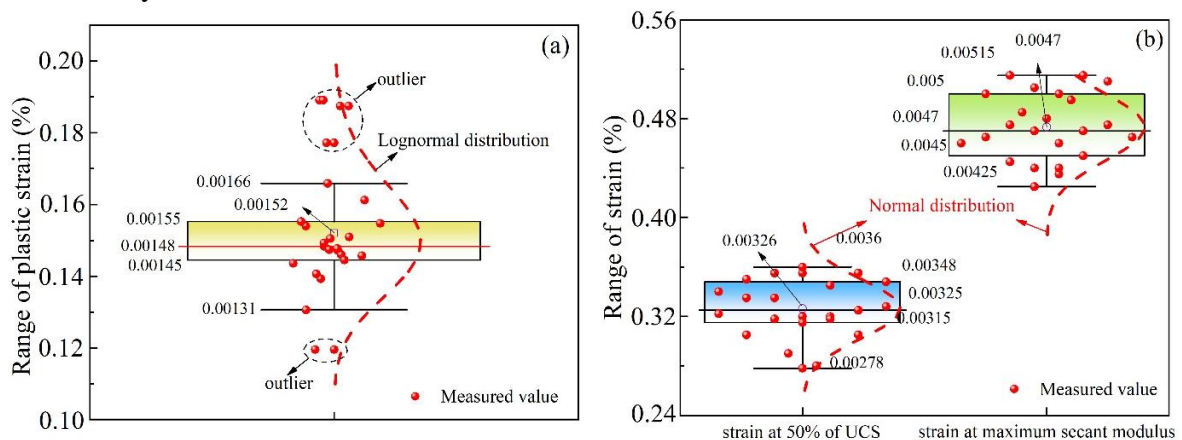
320 It can be seen from the results in Sections 3.3 and 3.4 that, with increasing water
 321 saturation, the plastic strain, the strain corresponding to the E_{50} , and the maximum secant
 322 modulus are discrete distributions. The laws of distribution of these three variables were
 323 studied as follows.

324 First, the degrees of dispersion and laws of distribution of the three strains were analyzed
 325 by using a box plot [46-47]. A typical box plot is shown in Figure 10. The distribution range
 326 of a group of data can be intuitively determined using the box plot, and the form of distribution
 327 of the data set can also be preliminarily determined. Data points that exceed the upper and
 328 lower boundaries of the box plot are considered abnormal values.



329
 330 Figure 10: Box plot.

331 The box plots of the plastic strain, the strain at the E_{50} , and the strain at the maximum
 332 secant modulus are shown in Figure 11. Figure 11a shows the box plot of the plastic strain,
 333 which shows that most of the plastic strains of the specimens with different water saturations
 334 were distributed within the upper and lower edges. There were a total of 16 data points, of
 335 which 11 were distributed within the range of the box body from 0.00155 to 0.00145, so it can
 336 be preliminarily determined that the plastic strain followed a normal distribution. Figure 11b
 337 is the box plot of the strain corresponding to 50% of the UCS and the strain corresponding to
 338 the maximum secant modulus. It can be seen from Figure 10b that the data points for both
 339 strains were within the upper and lower edges, there were no abnormal points, and the average
 340 values and median lines of both strains were almost equal, indicating that the two groups of
 341 data have better concentrations. The strain at 50% of the UCS was mostly distributed in the
 342 range of 0.00315-0.00348. There were 13 points in total, with five data points between the
 343 upper quartile and the upper edge and five between the lower quartile and the lower edge. The
 344 strain at the maximum secant modulus was primarily distributed in the range of 0.0045-0.005.
 345 There were 14 data points in total, with four data points between the upper quartile and the
 346 upper edge and five between the lower quartile and the lower edge. Therefore, it can be
 347 preliminarily determined that the two strains conformed to the normal distribution.

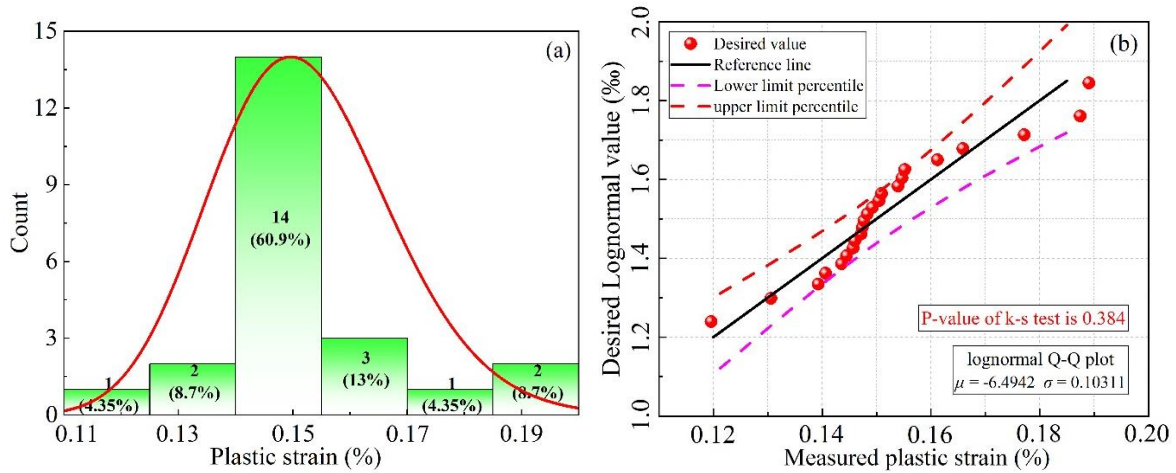


348
 349 Figure 11: Box plots of (a) plastic strain and (b) strain at E_{50} and maximum secant modulus.

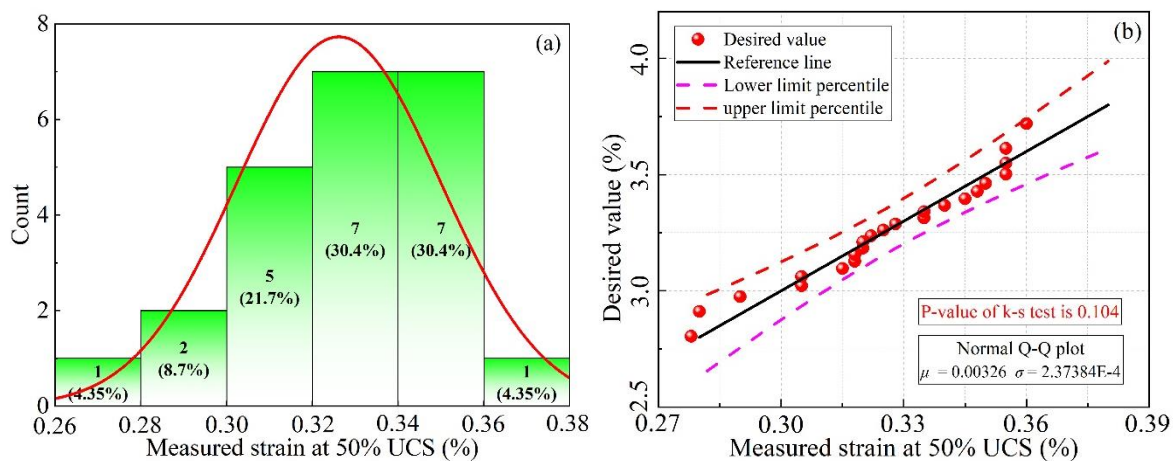
350 To further determine the distribution of the three strains, a distribution histogram and a
 351 Q-Q plot of each strain were developed, as shown in Figure 12-14. Figure 12 is the distribution

352 histogram of the plastic strain, which shows that most of the plastic strains were concentrated
 353 between 0.00140 and 0.00155, accounting for 60.9% of the total. There were few other interval
 354 distributions, but, due to its non-symmetric distribution, the plastic strain was closer to a
 355 lognormal distribution. It can also be seen from Figure 12b that most of the data points were
 356 distributed along the reference line. Using the K-S test, the P-value was 0.384, which is greater
 357 than the 0.05 reference value, indicating that it conformed to the typical lognormal distribution
 358 characteristics. Similarly, the strain at 50% of the UCS and the strain at the maximum secant
 359 modulus underwent distribution fitting and the K-S test, which indicated that both conformed
 360 to the normal distribution. The strain at 50% of the UCS was mostly concentrated in the range
 361 of 0.0032 to 0.0034 and 0.0034 to 0.0036; the total of the two accounted for 60.8%; the P-value
 362 was 0.107. The strain at the maximum secant modulus was mostly distributed in the range of
 363 0.0046 to 0.0048, and the P-value was 0.469. The P-values of the two types of strains were
 364 greater than 0.005, indicating that they conformed to the typical normal distribution
 365 characteristics.

366 In summary, the three types of strain data all conformed to the normal distribution,
 367 indicating that the relationships between the three types of strain and the water saturation are
 368 independent of each other, i.e., the water saturation will not be affected by these three types of
 369 strain.



370 Figure 12: Plastic strain. (a) Histogram. (2) Q-Q plot.



372 Figure 13: Strain at 50% of the UCS. (a) Histogram. (2) Q-Q plot.

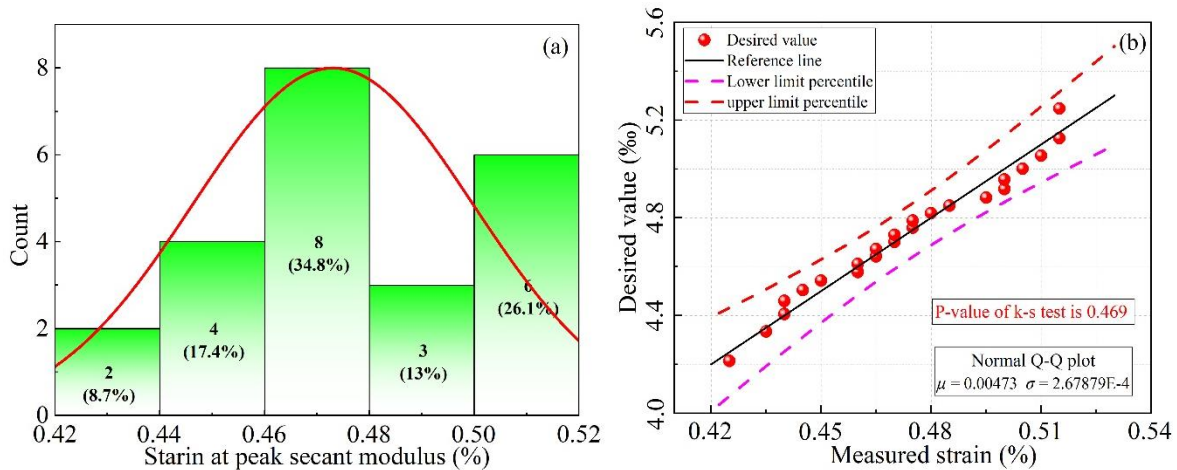


Figure 14: Strain at the maximum secant modulus. (a) Histogram. (2) Q-Q plot.

374
375

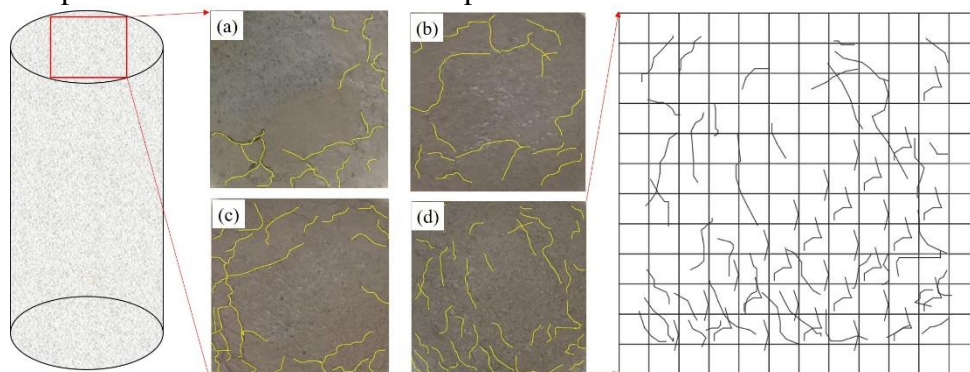
376 4.3 Mechanism of CPB strength degradation

377 The results in Sections 3.1 and 4.1 show that the peak stress of the CPB decreased
378 exponentially with increasing water saturation, and the CPB strength difference between
379 different water saturations decreased exponentially as the water saturation increased. Because
380 CPB and concrete are both mixtures made of cement, particles, and water mixed in certain
381 ratios, there are many similarities in their water saturation characteristics [48-50].

382 There are two principals' reasons for the strength change of the CPB with varying water
383 saturation: the chemical corrosive action of water and the mechanical action of water. Due to
384 the long curing time (60d), the internal hydration process was completed, and the chemical
385 reaction had little effect on the strength. Thus, the strength difference was chiefly caused by
386 the physical effects of the water. During the CPB drying process, the water in the inner
387 capillaries gradually evaporated, and the capillaries shrank, resulting in an increase in capillary
388 suction in the CPB. When the CPB was treated with water saturation, capillary expansion was
389 caused by the continuous penetration of the water into the internal capillary, and the capillary
390 suction in the CPB was gradually reduced, resulting in an overall strength reduction.
391 Additionally, the water permeation led to the loosening of the overall structure of the CPB and
392 the deterioration of the overall strength of the CPB.

393 4.4 Distribution characteristics of cracks

394 Figure 15 shows the surface crack distribution of the CPB specimens with different water
395 saturations. It can be seen from Figure 15 that increased water saturation led to an increased
396 number and density of cracks. It can also be observed that most of the cracks were distributed
397 around the CPB specimens' peripheries, and, with increasing water saturation, the cracks
398 extended deeper into the center of the CPB specimens.



399

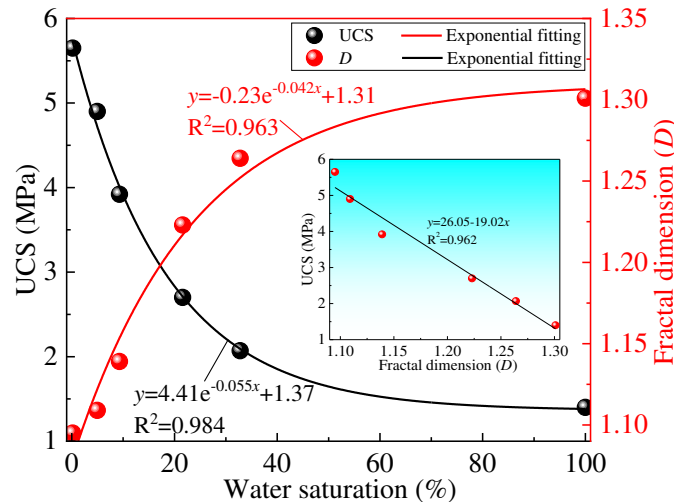
400 Figure 15: Distribution of the cracks in the CPB specimens with various water saturations. (a) 4.98%; (b)
401 9.32%. (c) 21.6%. (d) 32.8%.

402 With the help of fractal theory [51-52], the fractal dimensions of the crack outlines in the
403 CPB specimens with different water saturations were determined by the box-counting method,
404 and the results are shown in Figure 16. It can be seen that the cracks in the CPB specimens
405 with different water saturations demonstrated fractal characteristics. The fractal dimension, D ,
406 increased with increasing water saturation, and the change in the fractal dimension, D , is
407 inverse to the change in strength. Using exponential, logarithmic, and power functions to fit
408 the relationship between the fractal dimension and water saturation, it was found that the degree
409 of fit of the exponential function was the highest. This revealed that the relationship between
410 the fractal dimension of the cracks and the water saturation is an exponential function,
411 expressed as:

$$D = -0.23e^{-0.042w_s} + 1.31 \quad (14)$$

412 where D is the fractal dimension of the cracks in the CPB.

413 Further, the relationship between the UCS of the CPB and its fractal dimension was
414 obtained, as shown in Figure 16. It was found that the UCS of the CPB decreased with
415 increasing fractal dimension, and R^2 was as high as 0.962 with linear fitting, demonstrating
416 that they have a good linear function relationship.
417



418
419

Figure 16: Relationship between the water saturation and the fractal dimension.

420 5. Conclusions

421 Water saturation has a great influence on the mechanical properties of CPB. In this paper,
422 uniaxial compression tests were carried out on five kinds of CPB specimens with different
423 water saturation. The influence of water saturation on CPB strength, deformation and apparent
424 crack was discussed. Based on the research of this paper, the main conclusions are as follows:

425 (1) The deformation modulus of the CPB decreased with increasing water saturation.
426 After the peak point, the strength of the CPB decreased rapidly when the water saturation was
427 less than 20%, and the strength decreased slowly when the water saturation was greater than
428 30%.

429 (2) The relationship between the water saturation and the UCS, residual strength, peak
430 strain, elastic strain, and strain ratio had an exponential function: $y = a_1e^{b_1x} + c_1$. The UCS,
431 residual strength, peak strain, and elastic strain of the CPB decreased and the strain ratio of the
432 CPB increased with increasing water saturation. There was no apparent relationship between
433 the plastic strain and water saturation.

434 (3) The secant modulus of the CPB decreased with increasing the water saturation, and it
 435 first increased and then decreased (the critical point was 0.5%) with increasing strain. The E_{50}
 436 decreased with increasing water saturation as an exponential function: $y = a_3 + b_3 e^{c_3 x}$.

437 (4) The strength difference of the CPB decreased with increasing water saturation, and
 438 there was a strong exponential function relationship between them. The water saturation had
 439 little effect on the plastic strain, the E_{50} strain, or the maximum secant modulus strain.

440 (5) Most of the cracks in the CPB specimens with different water saturations were
 441 distributed around the periphery of the specimens. The greater the water saturation was, the
 442 more cracks that were present in the CPB. The fractal dimension, D , of the cracks in the CPB
 443 increased exponentially with increasing water saturation. The fractal dimension, D , has a
 444 negative linear correlation with the UCS.

445 This study considered the effects of water saturation on the mechanical properties of CPB
 446 and demonstrated that water saturation has apparent degradative effects on the mechanical
 447 properties of CPB. However, the influence of water saturation on the mechanical properties of
 448 CPB is closely related to the cement-to-tailings ratio, slurry concentration, and curing age,
 449 among other factors. This study can provide a scientific reference for the strength design of
 450 CPB when the underground is rich in water.

451 1. Author Contributions

452 J.W. and J.F. analyzed the experimental data and initiated the writing of the paper; W.D.
 453 modified the manuscript; Y.Z. corrected the English writing.

454 2. Funding Statement

455 This research was supported the National Natural Science Foundation of China (Grant
 456 No. 51974012), the National Natural Science Foundation of China Youth Fund (51804016),
 457 and the Fundamental Research Funds for the Central Universities (FRF-BD-19-005A).

458 3. Acknowledgments

459 The experimental works described in this study were conducted at the Key Laboratory of
 460 High-Efficient Mining and Safety of Metal Mines of the Ministry of Education in the
 461 University of Science and Technology Beijing. The authors gratefully acknowledge the staff
 462 and students at the laboratory for technical help during testing.

463 4. Conflicts of Interest

464 The authors declare that there is no conflict of interest regarding the publication of this
 465 paper.

466 5. References

- 467 [1] A. Tariq, E.K. Yanful, A review of binders used in cemented paste tailings for underground and
 468 surface disposal practices, *J. Environ. Manag.* 131 (8) (2013) 138-149.
- 469 [2] C. Qi, A. Fourie, Q. Chen, Neural network and particle swarm optimization for predicting the
 470 unconfined compressive strength of cemented paste backfill, *Constr. Build. Mater.* 159 (2018) 473–
 471 478.

- 472 [3] L. Liu, Z.Y. Fang, C.C. Qi, B. Zhang, L.J. Guo, K.I. Song. Experimental investigation on the
473 relationship between pore characteristics and unconfined compressive strength of cemented paste
474 backfill, *Constr. Build. Mater.* 179 (2018) 254-264.
- 475 [4] W. Zhu, J. Xu, J. Xu, D. Chen, J. Shi, Pier-column backfill mining technology for controlling surface
476 subsidence, *Int. J. Rock Mech. Min. Sci.* 96 (2017) 58-65.
- 477 [5] W. Sun, H.J. Wang, K.P. Hou, Control of waste rock-tailings paste backfill for active mining
478 subsidence areas, *Journal of Cleaner Production.* 171 (10) (2018) 567-579.
- 479 [6] X. Li, J. Du, L. Gao, S. He, L. Gan, C. Sun, Y. Shi, Immobilization of phosphogypsum for cemented
480 paste backfill and its environmental effect, *J. Clean. Prod.* 156 (2017) 137-146.
- 481 [7] L. Li, M. Aubertin, Numerical Investigation of the Stress State in Inclined Backfilled Stopes,
482 *International Journal of Geomechanics.* 9 (2) (2009) 52-62.
- 483 [8] G.L. Xue, E. Yilmaz, W.D. Song, E. Yilmaz, Influence of fiber reinforcement on mechanical behavior
484 and microstructural properties of cemented tailings backfill, *Construction and Building Materials.* 213
485 (2019) 275-285.
- 486 [9] S.H. Yin, Y.J. Shao, A.X. Wu, Z.Y. Wang, L.H. Yang, Assessment of expansion and strength
487 properties of sulfidic cemented paste backfill cored from deep underground stopes, *Construction and*
488 *Building Materials.* 230 (2020) 116983.
- 489 [10] C.D. Min, X.B. Li, S.Y. He, S.T. Zhou, S. Yang, Y. Shi, Effect of mixing time on the properties of
490 phosphogypsum-based cemented backfill, *Construction and Building Materials.* 210 (20) (2019) 564-
491 573.
- 492 [11] P. Yang, L. Li, Investigation of the short-term stress distribution in stopes and drifts backfilled with
493 cemented paste backfill, *Int. J. Min. Sci. Technol.* 25 (05) (2015) 721-728.
- 494 [12] D.R. Tesarik, J.B. Seymour, T.R. Yanske., Long-term stability of a backfilled room-and-pillar test
495 section at the Buick Mine, Missouri, USA, *Int. J. Rock Mech. Min. Sci.* 46 (7) (2009) 1182-1196.
- 496 [13] Q.L. Yao, F.T. Zhang, X.L. Ding, L. Zhang, G. Jiang, Experimental research on instability mechanism
497 of silty mudstone roofs under action of water and its application, *Procedia Earth Planet. Sci.* 1 (1)
498 (2009) 402-408.
- 499 [14] M. Li, J.X. Zhang, Z. Liu, X. Zhao, P. Huang, Mechanical analysis of roof stability under nonlinear
500 compaction of solid backfill body, *International Journal of Mining Science and Technology.* 26 (5)
501 (2016) 863-868.
- 502 [15] X.Y. Zhang, M.Y. Xu, L. Liu, C. Huan, Y.J. Zhao, C.C. Qi. Experimental study on thermal and
503 mechanical properties of cemented paste backfill with phase change material, *Journal of Materials*
504 *Research and Technology.* 9 (2) (2020) 2164-2175.
- 505 [16] L.H. Yang, H.J. Wang, A.X. Wu, H. Li, T. Bruno, X. Zhou, X.T. Wang, Effect of mixing time on
506 hydration kinetics and mechanical property of cemented paste backfill, *Construction and Building*
507 *Materials.* 247 (30) (2020) 118516.
- 508 [17] J.F. Hou, Z.P. Guo, W.Z. Liu, Y.X. Zhang, Mechanical properties and meso-structure response of
509 cemented gangue-fly ash backfill with cracks under seepage- stress coupling, *Construction and Building*
510 *Materials.* 250 (30) (2020) 118863.
- 511 [18] M.B.C. Mangane, R. Argane, R. Trauchessec, A. Lecomte, M. Benzaazoua, Influence of
512 superplasticizers on mechanical properties and workability of cemented paste backfill, *Minerals*
513 *Engineering.* 116 (15) (2018) 3-14.

- 514 [19] Y.H. Zhang, X.M. Wang, C. Wei, Q.L. Zhang, Dynamic mechanical properties and instability behavior
515 of layered backfill under intermediate strain rates, *Transactions of Nonferrous Metals Society of China*.
516 27 (7) (2017) 1608-1617.
- 517 [20] M. Benzaazoua, J.F. Fiset, B. Bussiere, M. Villeneuve, B. Plante, Sludge recycling within cemented
518 paste backfill: Study of the mechanical and leachability properties, *Minerals Engineering*. 19 (2006)
519 420-432.
- 520 [21] S. Cao, W.D. Song, E. Yilmaz, Influence of structural factors on uniaxial compressive strength of
521 cemented tailings backfill, *Construction and Building Materials*. 174 (2018) 190-201.
- 522 [22] S. Cao, W.D. Song, Effect of filling interval time on the mechanical strength and ultrasonic properties
523 of cemented coarse tailing backfill, *International Journal of Mineral Processing*. 166 (2017) 62-68.
- 524 [13] M. Full, M. Benzaazoua, Modeling the effect of sulphate on strength development of paste backfill and
525 binder mixture optimization, *Cement and Concrete Research*. 35 (2005) 301-314.
- 526 [24] Z.X. Liu, T. Luo, X. Li, X.B. Li, Z. Huai, S.F. Wang, Construction of reasonable pillar group for
527 undersea mining in metal mine, *Transactions of Nonferrous Metals Society of China*. 28 (4) (2018)
528 757-765.
- 529 [25] W.Z. Liang, G.Y. Zhao, H. Wu, Y. Chen, Optimization of mining method in subsea deep gold mines: A
530 case study, *Transactions of Nonferrous Metals Society of China*. 29 (10) (2019) 2160-2169.
- 531 [26] B. Liu, Y.T. Gao, A.B. Jin, X. Wang, Influence of water loss on mechanical properties of superfine
532 tailing-blast-furnace slag backfill, *Construction and Building Materials*. 246 (20) (2020) 118482.
- 533 [27] A.X. Wu, Y. Wang, H.J. Wang, S.H. Yin, X.X. Miao, Coupled effects of cement type and water quality
534 on the properties of cemented paste backfill, *International Journal of Mineral Processing*. 143 (10)
535 (2015) (65-71).
- 536 [28] J.P. Zuo, Z.J. Hou, Z.Q. Xiong, C. Wang, H.Q. Song, Influence of different W/C on the performances
537 and hydration progress of dual liquid high water backfilling material, *Construction and Building*
538 *Materials*. 190 (30) (2018) 910-917.
- 539 [29] D.Y. Wei, C.F. Du, Y.F. Lin, B.M. Chang, Impact factors of hydration heat of cemented tailings
540 backfill based on multi-index optimization, *Case Studies in Thermal Engineering*. 18 (2020) 100601.
- 541 [30] J.R. Zheng, X.X. Sun, L.J. Guo, S.M. Zhang, J.Y. Chen, Strength and hydration products of cemented
542 paste backfill from sulphide-rich tailings using reactive MgO-activated slag as a binder, *Construction*
543 *and Building Materials*. 203 (10) (2019) 111-119.
- 544 [31] S.J. Chen, Z.W. Du, Z. Zhang, H.W. Zhang, Z.G. Xia, F. Feng, Effects of chloride on the early
545 mechanical properties and microstructure of gangue-cemented paste backfill, *Construction and*
546 *Building Materials*. 235 (28) (2020) 117504.
- 547 [32] L. Liu, C. Zhu, C.C. Qi, B. Zhang, K. Song, A microstructural hydration model for cemented paste
548 backfill considering internal sulfate attacks, *Construction and Building Materials*. 211 (30) (2019) 99-
549 108.
- 550 [33] D. Wu, Y.L. Zhang, C. Wang, Modeling the thermal response of hydrating cemented gangue backfill
551 with admixture of fly ash, *Thermochimica Acta*. 623 (10) (2016) 86-94.
- 552 [34] Y. Zhao, A. Taheri, M. Karakus, Z.W. Chen, A. Deng, Effects of water content, water type and
553 temperature on the rheological behaviour of slag-cement and fly ash-cement paste backfill,
554 *International Journal of Mining Science and Technology*. 2020 In press.

- 555 [35] Y.L. Nie, X.J. Wang, G.L. Huang, S.C. Li, X. Feng, S.R. Cao, Strength and Damage Model Analysis of
556 Pure Tailings Cemented Filling Body with Different Water Content. *Bulletin of the Chinese Ceramic*
557 *Society*. 37 (6) (2018) 2008-2013.
- 558 [36] J.W. Liu, W.H. Sui, D.Y. Zhang, Q.J. Zhao, Durability of water-affected paste backfill material and its
559 clean use in coal mining, *Journal of Cleaner Production*. 250 (2020) 119576.
- 560 [37] Y.Q. Hou, Y.P. Zhang, L. Wang, X.G. Zou, Research on dynamic load failure characteristics of dry and
561 saturated backfill, *Industrial Minerals & Processing*. 7 (2017) 38-45.
- 562 [38] A. Rabat, M. Cano, R. Tomas, Effect of water saturation on strength and deformability of building
563 calcarenite stones: Correlations with their physical properties, *Construction and Building Materials*.
564 232 (2020) 117259.
- 565 [39] L. Zhuang, K.Y. Kim, M. Diaz, S. Yeom, Evaluation of water saturation effect on mechanical
566 properties and hydraulic fracturing behavior of granite, *International Journal of Rock Mechanics and*
567 *Mining Sciences*. 130 (2020) 104321.
- 568 [40] X.J. Du, G.R. Feng, T.Y. Qi, Y.X. Guo, Y.J. Zhang, Z.H. Wang, Failure characteristics of large
569 unconfined cemented gangue backfill structure in partial backfill mining, *Construction and Building*
570 *Materials*. 194 (2019) 257-265.
- 571 [41] A. Torok, B. Vasarhelyi, The influence of fabric and water content on selected rock mechanical
572 parameters of travertine, examples from Hungary, *Eng. Geol.* 115 (3-4) (2010) 237-245.
- 573 [42] A.R. Najibi, M. Ghafoori, G.R. Lashkaripour, M.R. Asef, Empirical relations between strength and
574 static and dynamic elastic properties of Asmari and Sarvak limestones, two main oil reservoirs in Iran,
575 *J. Pet. Sci. Eng.* 126 (2015) 78-82.
- 576 [43] V. Brotons, R. Tomás, S. Ivorra, A. Grediaga, Relationship between static and dynamic elastic modulus
577 of calcarenite heated at different temperatures: the San Julián's stone, *Bull. Eng. Geol. Environ.* 73 (3)
578 (2014) 791-799.
- 579 [44] A.B. Hawkins, B.J. McConnell, Sensitivity of sandstone strength and deformability to changes in
580 moisture content, *Quarterly J. Eng. Geology*. 25 (1992) 115-130.
- 581 [45] B. Vásárhelyi, Some observations regarding the strength and deformability of sandstones in case of dry
582 and saturated conditions, *Bull. Eng. Geol. Env.* 62 (2003) 245-249.
- 583 [46] S. Lem, P. Onghena, L. Verschaffel, W.V. Dooren, The heuristic interpretation of box plots, *Learning*
584 *and Instruction*. 26 (2013) 22-35.
- 585 [47] H.F.J. Theart, R. Ghavami-Riabi, H. Mouri, P. Graser, Applying the box plot to the recognition of
586 footwall alteration zones related to VMS deposits in a high-grade metamorphic terrain, South Africa, a
587 lithochemical exploration application, *Geochemistry*. 71 (2) (2011) 143-154.
- 588 [48] J.M. Torrenti, L. Granger, M. Diruy, P. Genin, 1997. Modélisation du retrait du béton en ambiance
589 variable, *Revue Française de Génie Civil*. 1 (4) (1997) 687-698.
- 590 [49] I. Yurtdas, N. Burlion, F. Skoczylas, Experimental characterisation of the drying effect on uniaxial
591 mechanical behavior of mortar, *Materials and Structures*. 37 (267) (2004) 170-176.
- 592 [50] N. Burlion, F. Bourgeois, J.F. Shao, Effects of desiccation on mechanical behavior of concrete, *Cement*
593 *and Concrete Composites*. 27 (3) (2005) 367-379.

- 594 [51] T. Liu, X.N. Zhang, Z. Li, Z.Q. Chen, Research on the homogeneity of asphalt pavement quality using
595 X-ray computed tomography (CT) and fractal theory, *Construction and Building Materials*. 68 (2014)
596 587-598.
- 597 [52] J.M. Wang, L.L. Guo, Z.K. Bai, L.L. Yang, Using computed tomography (CT) images and multi-fractal
598 theory to quantify the pore distribution of reconstructed soils during ecological restoration in opencast
599 coal-mine, *Ecological Engineering*. 92 (2016) 148-157.

Figures

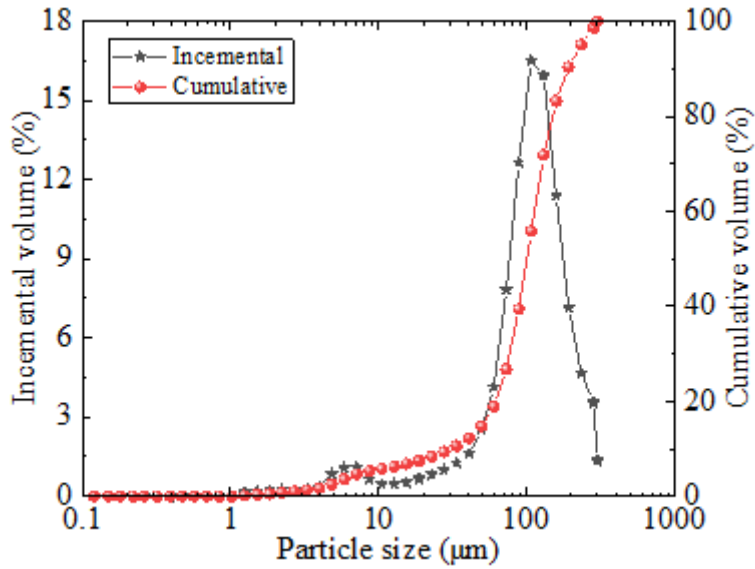


Figure 1

Incremental and cumulative PSD curves of the tailings.

Group	Number	Water saturation process	
		Step 1	Step 2
WS	5	2 weeks in curing box	UCS test in water
AD1	3	6d in oven of 105°C	1d in Lab → UCS test
AD	5		2 weeks in Lab → UCS test
IW	3	1d in Laboratory	2 weeks in Lab → 30s in water → UCS test
OD	3	Water saturation under vacuum state	6d in oven of 105 ° → UCS test
VD	5		1d in vacuum tub → UCS test

Figure 2

CPB specimen water saturation processes.



Figure 3

CPB specimens are sealed in plastic bags.

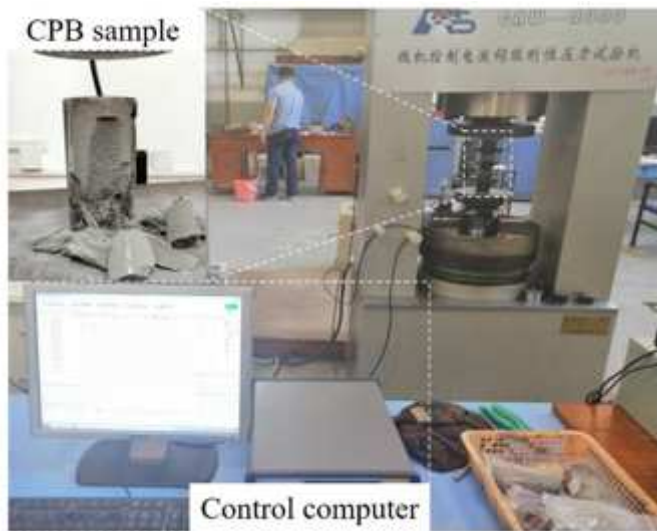


Figure 4

GAW-2000 electro-hydraulic servo testing machine.

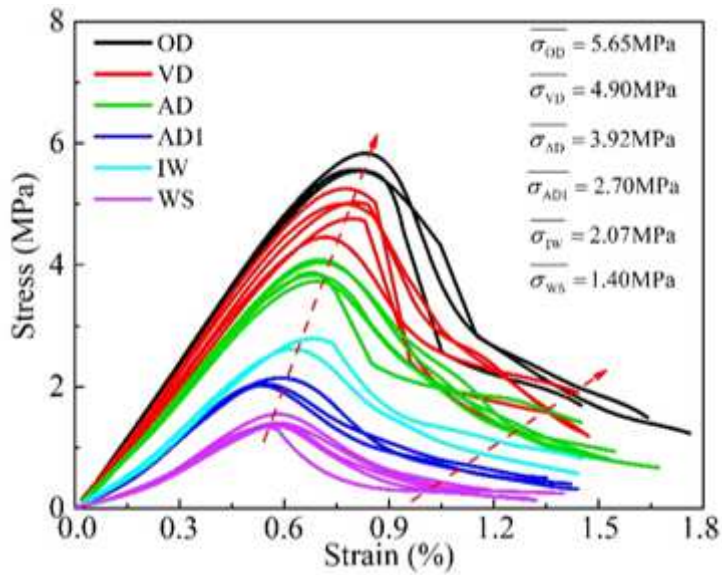


Figure 5

Stress-strain curve of the specimens with different water saturation values.

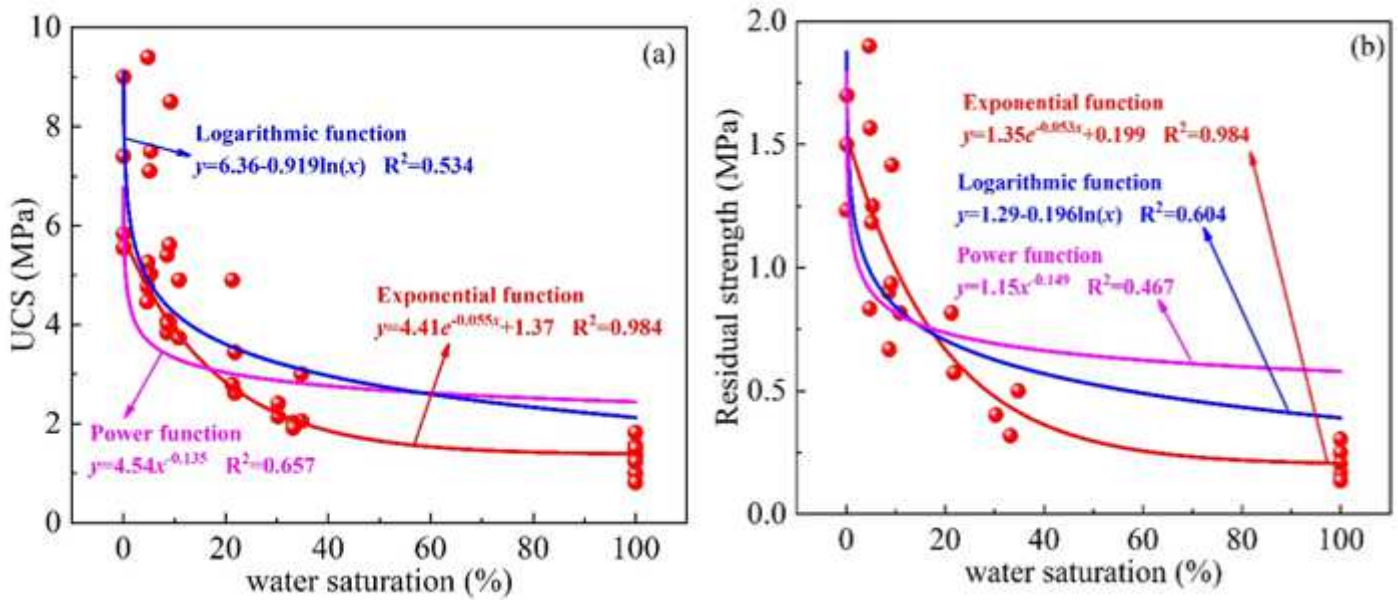


Figure 6

Relationship between the strength and water saturation of the CPB specimens. (a) UCS. (b) residual strength.

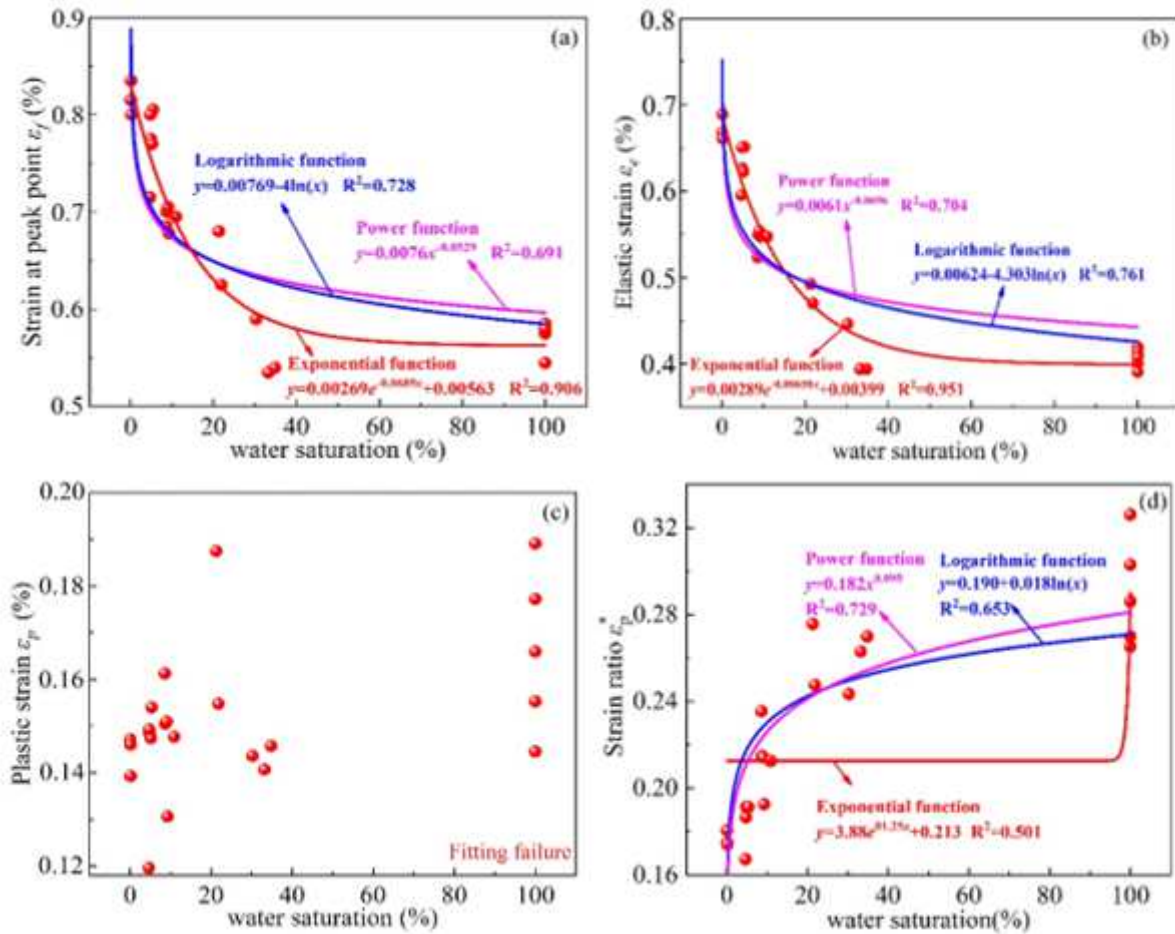


Figure 7

Relationship between the strains and water saturation. (a) ϵ_f . (b) ϵ_e . (c) ϵ_p . (d) ϵ_p^* .

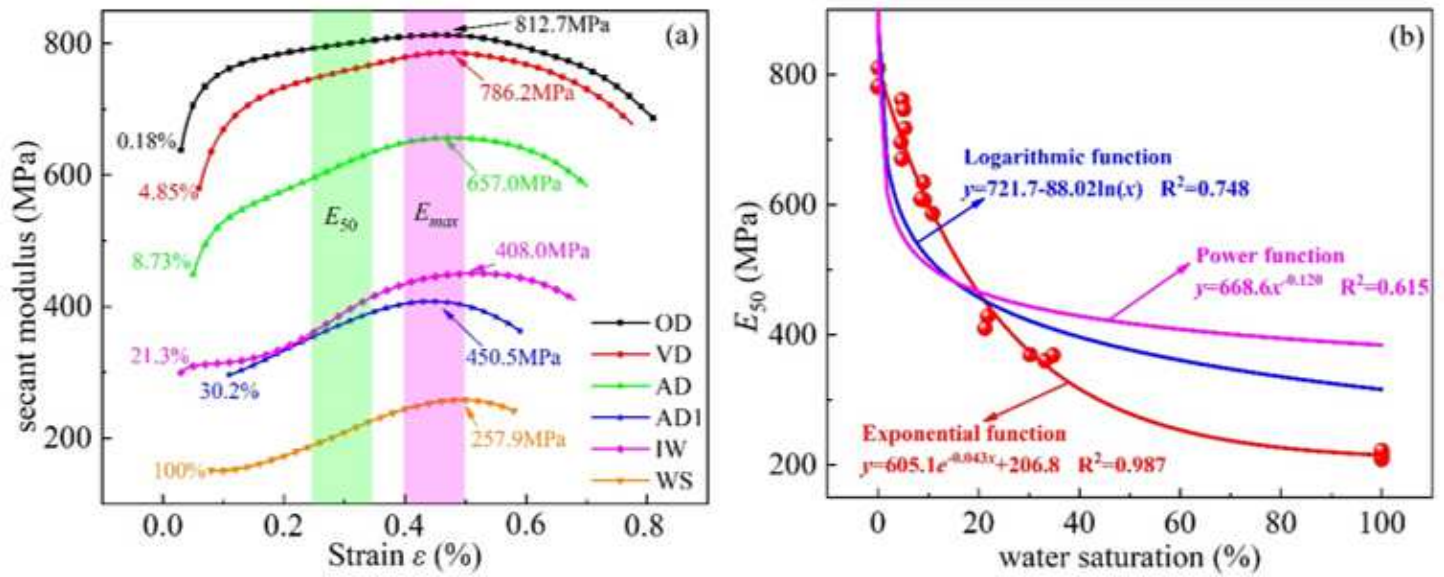


Figure 8

The evolution of the CPB modulus. (a) secant modulus. (b) E_{50} .

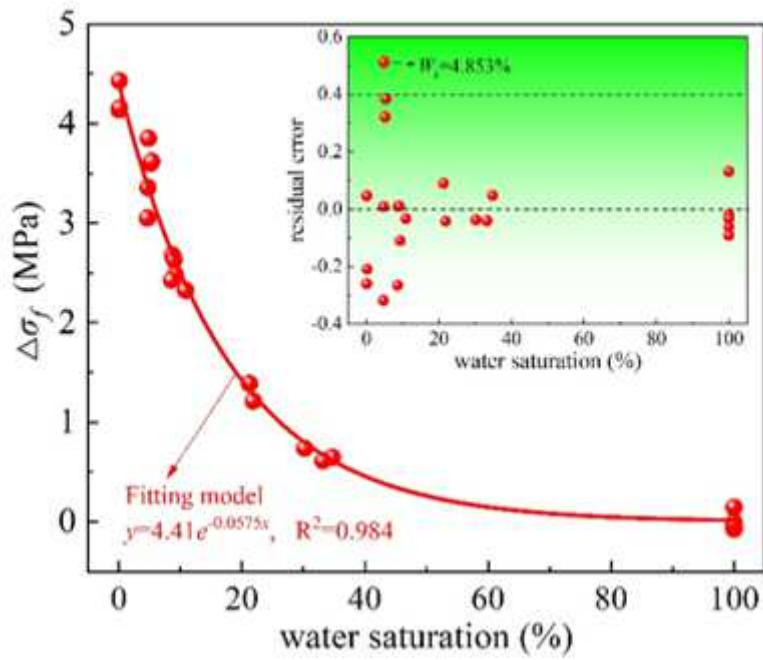


Figure 9

Relationship between the strength difference and water saturation.

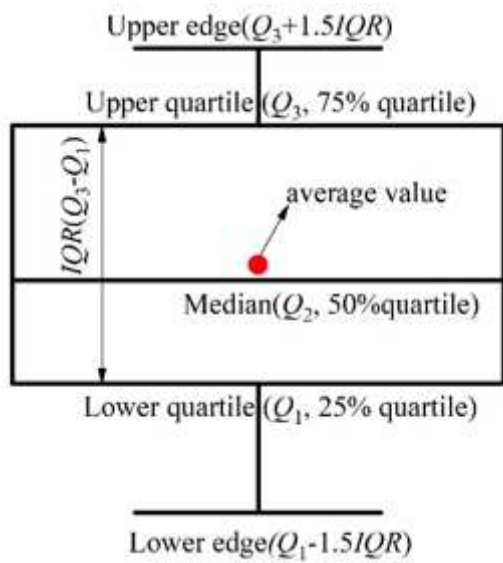


Figure 10

Box plot.

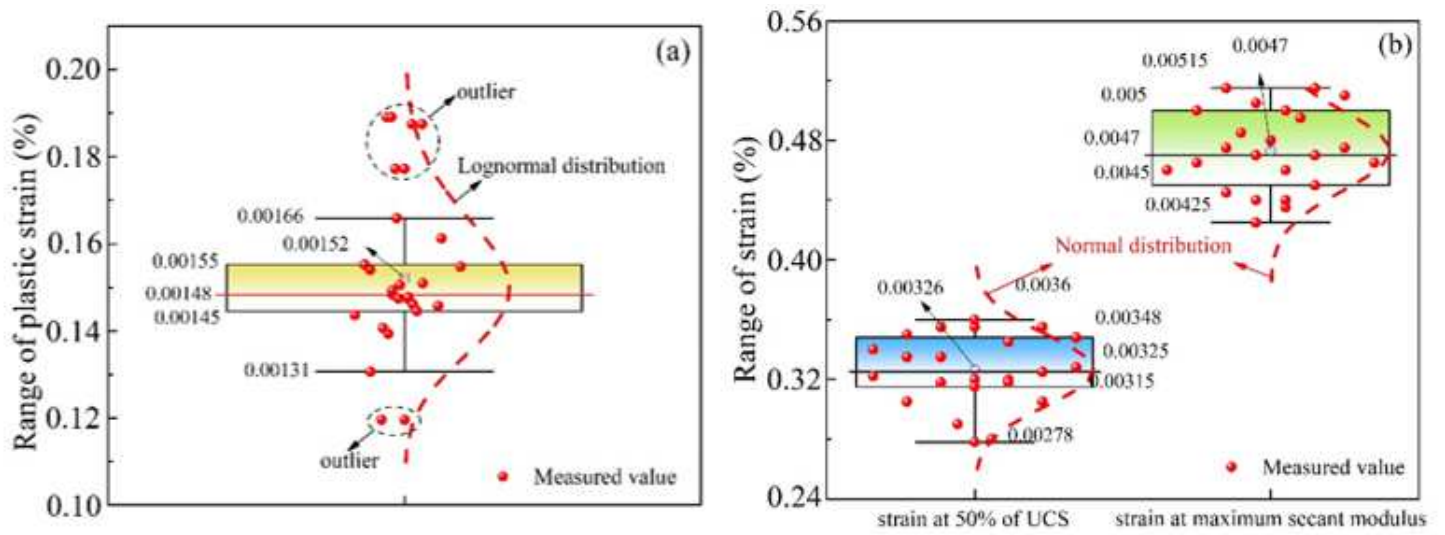


Figure 11

Box plots of (a) plastic strain and (b) strain at E50 and maximum secant modulus.

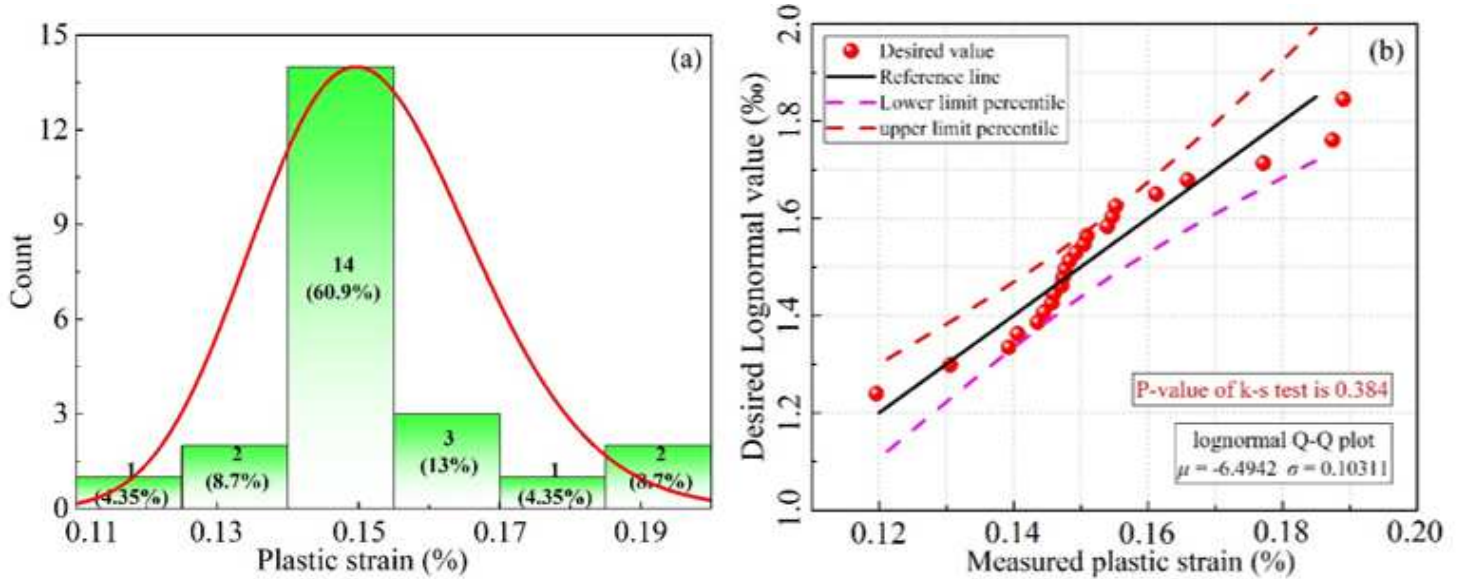


Figure 12

Plastic strain. (a) Histogram. (2) Q-Q plot.

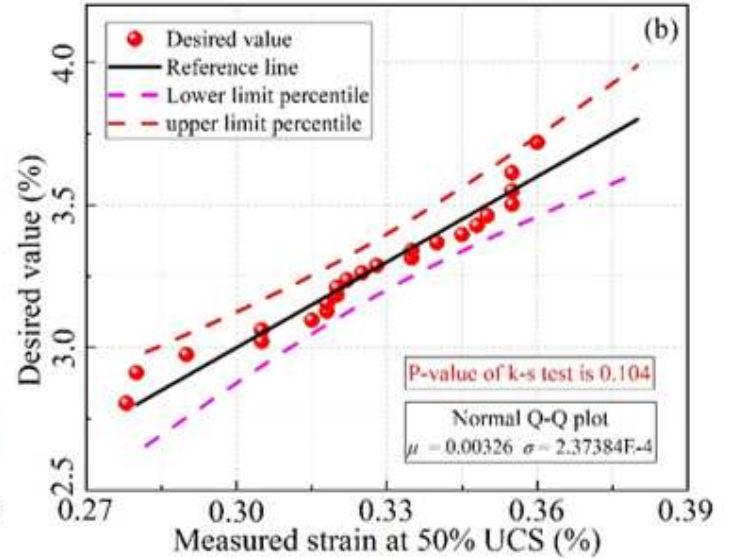
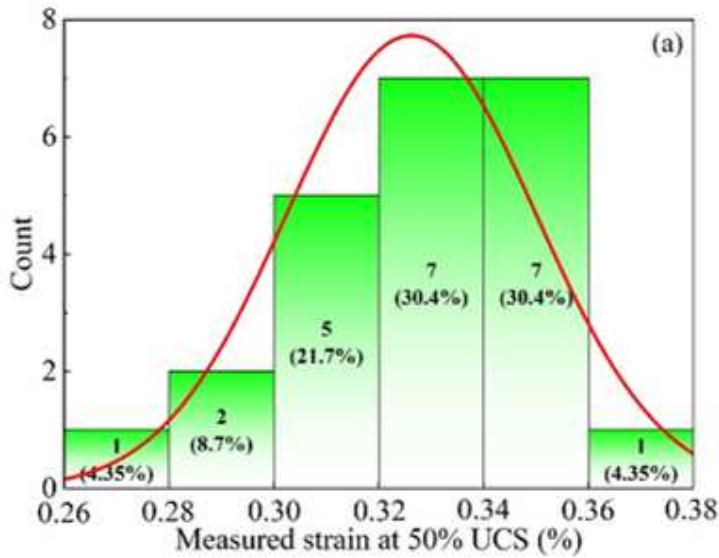


Figure 13

Strain at 50% of the UCS. (a) Histogram. (2) Q-Q plot.

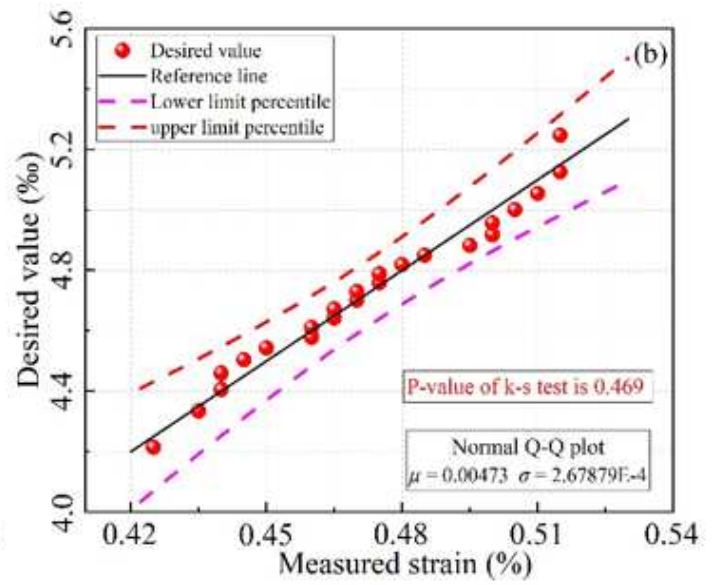
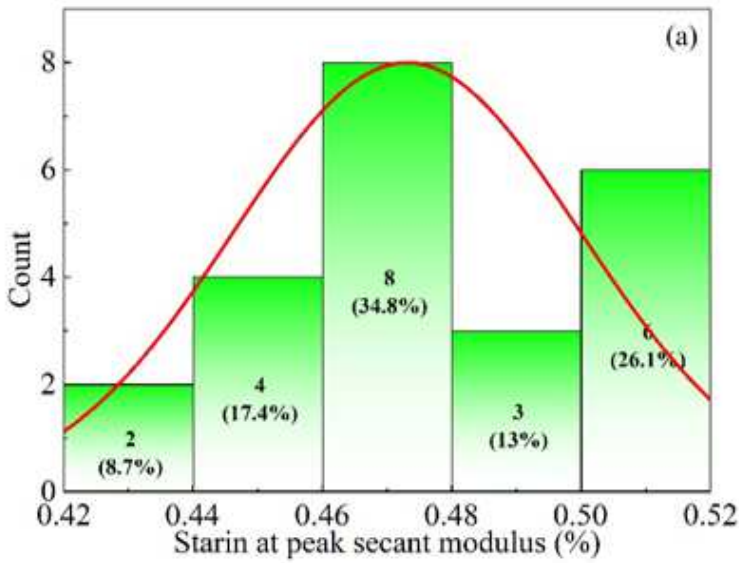


Figure 14

Strain at the maximum secant modulus. (a) Histogram. (2) Q-Q plot.

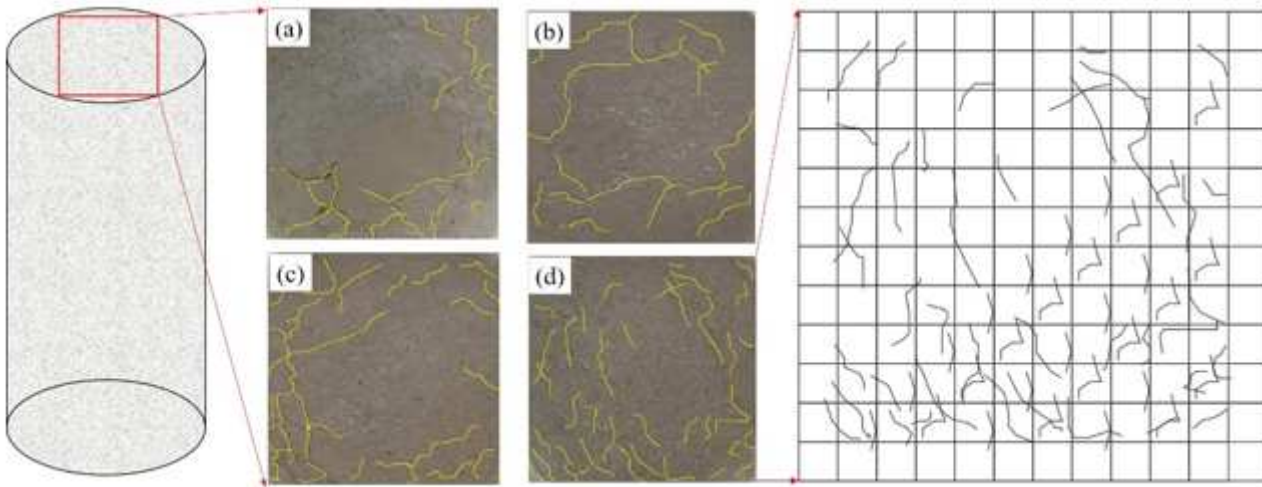


Figure 15

Distribution of the cracks in the CPB specimens with various water saturations. (a) 4.98%; (b) 9.32%. (c) 21.6%. (d) 32.8%.

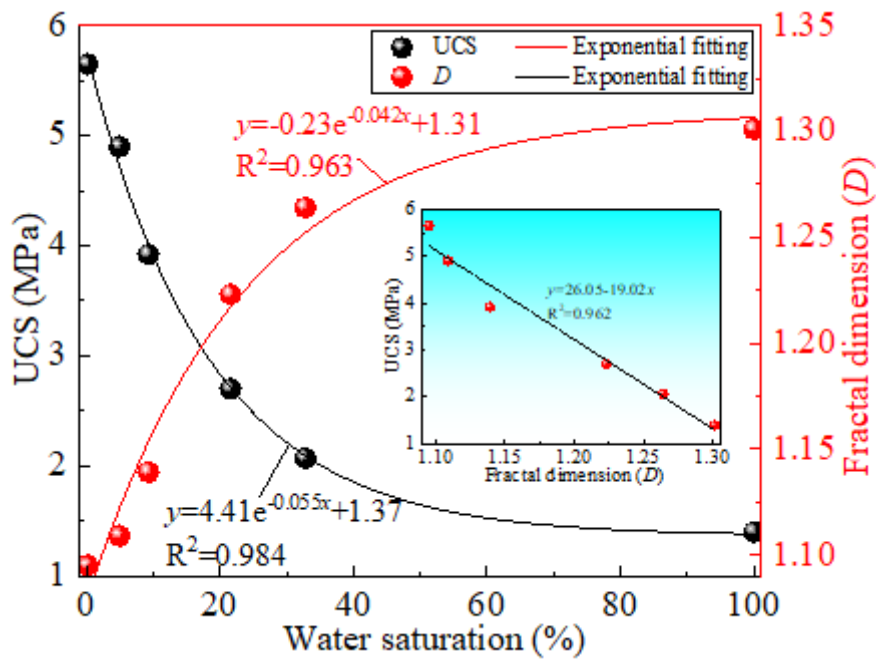


Figure 16

Relationship between the water saturation and the fractal dimension.